

## Article

# Design Optimization of Induction Motors with Different Stator Slot Rotor Bar Combinations Considering Drive Cycle

Farshid Mahmouditabar \*  and Nick J. Baker 

School of Engineering, Newcastle University, Newcastle upon Tyne NE1 7RU, UK; nick.baker@newcastle.ac.uk

\* Correspondence: farshid.mahmouditabar@newcastle.ac.uk

**Abstract:** In this paper, a sequential Taguchi method for design optimization of an induction motor (IM) for an electric vehicle (EV) is presented. First, a series of empirical and mathematical relationships is systematically applied to reduce the number of possible stator slot rotor bar (SSRB) combinations. Then, the admissible optimal combinations are investigated and compared using finite element (FE) simulation over the NEDC driving cycle, and the three best combinations are selected for further analysis. Each topology is optimized over the driving cycle using the k-means clustering method to calculate the representative working points over the NEDC, US06, WLTP Class 3, and EUDC driving cycles. Then, using the Design of Experiment (DOE)-based Taguchi method, a multi-objective optimization is carried out. Finally, the performance of the optimized machines in terms of robustness against manufacturing tolerances, magnetic flux density distribution, mechanical stress analysis, nominal envelope curve and efficiency map is carried out to select the best stator slot rotor bar combination. It is also found that the K-means clustering method is not completely robust for the design of electric machines for electric vehicle traction motors. The method focuses on regions with high-density working points, and it is possible to miss the compliant with the required envelope curve.

**Keywords:** induction motor; electric vehicle; systematic design; Taguchi; lumped parameter method; k-means; thermal design



**Citation:** Mahmouditabar, F.; Baker, N.J. Design Optimization of Induction Motors with Different Stator Slot Rotor Bar Combinations Considering Drive Cycle. *Energies* **2024**, *17*, 154. <https://doi.org/10.3390/en17010154>

Academic Editor: Daniel Morinigo-Sotelo

Received: 1 December 2023

Revised: 22 December 2023

Accepted: 25 December 2023

Published: 27 December 2023



**Copyright:** © 2023 by the authors. Licensee MDPI, Basel, Switzerland. This article is an open access article distributed under the terms and conditions of the Creative Commons Attribution (CC BY) license (<https://creativecommons.org/licenses/by/4.0/>).

## 1. Introduction

Governments are encouraging automotive manufacturers to develop electric vehicles (EVs) due to environmental concerns and future scarcity of fuel. High torque, accurate control, short acceleration times and high cruising speeds are requirements for electric vehicles that are directly tied to the characteristics of their electric motors. The proper design of the electric machines for EV applications should have the characteristics of high performance, high efficiency, low-cost, high-power density, extended flux weakening range, ease of manufacturing, and high reliability [1–5].

The interior permanent magnet (IPM) machine and the induction machine (IM) are the most advantageous topologies for EV traction motors. The IM has several advantages, including low cost, high reliability, easy controllability, and well-developed manufacturing technology. However, because of rotor copper losses, it has poor efficiency and low power factor at low speeds [2]. The IPM is more efficient and has a higher power density than the IM. However, its complex control method, increased cost, sensitive supply chain, and vulnerability to irreversible demagnetization (ID) are some of the challenges with widespread adoption of the IPM [3,6].

Both machines therefore have their own advantages and disadvantages. Previous studies reveal that delivering similar performance requires a larger IM with higher current ratings. Despite this, the technology is well established in the automotive industry (e.g., Tesla 60S, Audi e-tron) as a PM-free motor and could still represent an attractive and feasible solution for future EVs. The use of rare earth PMs can give significant concerns for

electric machine manufacturers in terms of cost, diversity of supply chain, cost volatility and long-term sustainability. Alternative materials used in electrical machines have a different impact level on the environment. To evaluate and compare their impact, an investigation study has been carried out in Sweden that includes an impact assessment (characterization and weighting) method for assigning a monetary value to emissions and the use of natural resource. The results of the study impact assessment method are ‘damage costs’ for emissions and the use of natural resources expressed as ELU (Environmental Load Units). ELU 1 corresponds to EUR 1 environmental damage cost. The ELU of goods is evaluated considering the ISO standards for life cycle assessment (LSA) (ISO 14044 [7] and ISO 14008 [8]), which is on the monetary valuation of environmental impacts. The details of ELU for used material in electrical machines is illustrated in Table 1 [9,10].

**Table 1.** ELU of common material used in electric machines [9,10].

Material	ELU/kg Material	Material	ELU/kg Material
Dysprosium	1500	Copper	131
Samarium	1160	Boron	9.10
Cobalt	205	Iron (steel)	1.00
Neodymium	202	Strontium	0.18
Lanthanum	175	Aluminum	0.16

Regarding ELU, the highest negative impact on the environment is associated with rare earth material (REM), due to its very energy intensive mining and environmentally damaging manufacturing processes. The processing of rare earth elements into high-purity rare-earth oxides requires significant experience in mineral processing [11]. Therefore, it is interesting to investigate alternative, potentially more sustainable electric machines.

One of the important aspects of sustainable design is increasing efficiency, thereby reducing the environmental impact during the operational lifetime. The proper design of electrical machines for EV applications must consider its working conditions, which can differ from that of other industrial applications. In conventional industrial applications, the electric motor can be designed to efficiently operate at one or two operating points. In EVs, however, the machine needs to operate at a wide range of speed–torque points. Therefore, for this application, the driving cycle should be considered in the design and optimization process. To increase the vehicle range and increase the efficiency of the vehicle, it is necessary to extend the region with the highest efficiency and locate the most efficient region where more operating points are located [12]. The number of operating points over the driving cycles can be several thousand. Performing the conventional FE-based optimization approaches can easily result in enormous computational time. Therefore, it is necessary to use some methods to reduce the number of operating points or use the developed analytical models to reduce the optimization time. Regarding reducing the number of operating points, approaches like Energy Center of Gravity [13], Geometric Center of Gravity [14,15], and k-means [10,16–18] clustering are utilized to convert the total working points of the machine to several representing points. In the second approach, the researcher used the analytical models instead of FE, as the computational time is significantly lower, and it is possible to consider all the operating points in the optimization procedure. The utilized analytical models for this purpose are the adaptive network-based fuzzy interface system model [19], reluctance circuit model [20], sub-domain analytical model [21], and meta-model-based approach [22].

Regarding the optimal selection of stator slot rotor bar (SSRB) combination, various articles for other industry applications can be found. The investigations have covered different combinations of SSRB from the point of view of noise [23], vibration, crawling, steady-state performance [24,25], rotor bar current waveform [26], etc.

Regarding the optimum shape design of stator slot and rotor bar of the IM, Ref. [27] examines the pulsating torque of an induction machine from the standpoint of designing appropriate stator slot and rotor bar dimensions. Ref. [28] presents the design principles

of an induction motor used in a hybrid EV, considering the effects of starting, operating performance, and harmonics. In [29], a parametric study was conducted to examine the effect of stator and rotor slot dimensions on various performance parameters, and an evolutionary algorithm was used for IM design optimization.

Regarding the design of IM for EV application, in [30], an optimization procedure has been introduced that can consider the overload capability of the IM over the driving cycle. The overload has been investigated by checking the hotspot temperature of the winding. In [31], a 200 kW 370 N.m IM has been designed for an EV with the target of enhancing the performance for mass production. To achieve this goal, suitable materials and manufacturing processes like rotor die-casting, hairpin stator winding, and a specific cooling system have been investigated. In [32], a low-cost totally enclosed fan IM with an aluminum-cage rotor IM has been designed for city battery EVs. In the optimization process, to accurately size the thermos-electromagnetic parts of the IM, the FE model and thermal model are coupled.

The contribution of this paper is presenting a systematic approach for the design optimization of IM over a driving cycle, considering different SSRB combinations. In the presented process, a series of empirical and mathematical relationships will be systematically applied to reduce the number of possible SSRB combinations. Then, the admissible optimal combinations will be investigated and compared over driving cycle using FE simulation. Finally, for the best three SSRB combinations the design optimization over driving cycle is presented.

The remainder of this article is organized as follows. In Section 2, the proposed design optimization algorithm is introduced and possible SSRB combinations are obtained. In Section 3, the initial design of the possible SSRB combinations is carried out and their performances are compared over the driving cycle. In Section 4, the design optimization of the best three SSRB combinations is carried out over the driving cycle using representing points calculated using the k-means clustering algorithm. Finally, a comprehensive performance evaluation of optimized IMs is carried out in Section 5, followed by the conclusion in Section 6.

## 2. The Proposed Design Procedure

The proposed design optimization algorithm is shown in Figure 1. The details of the proposed design optimization procedure are outlined below.

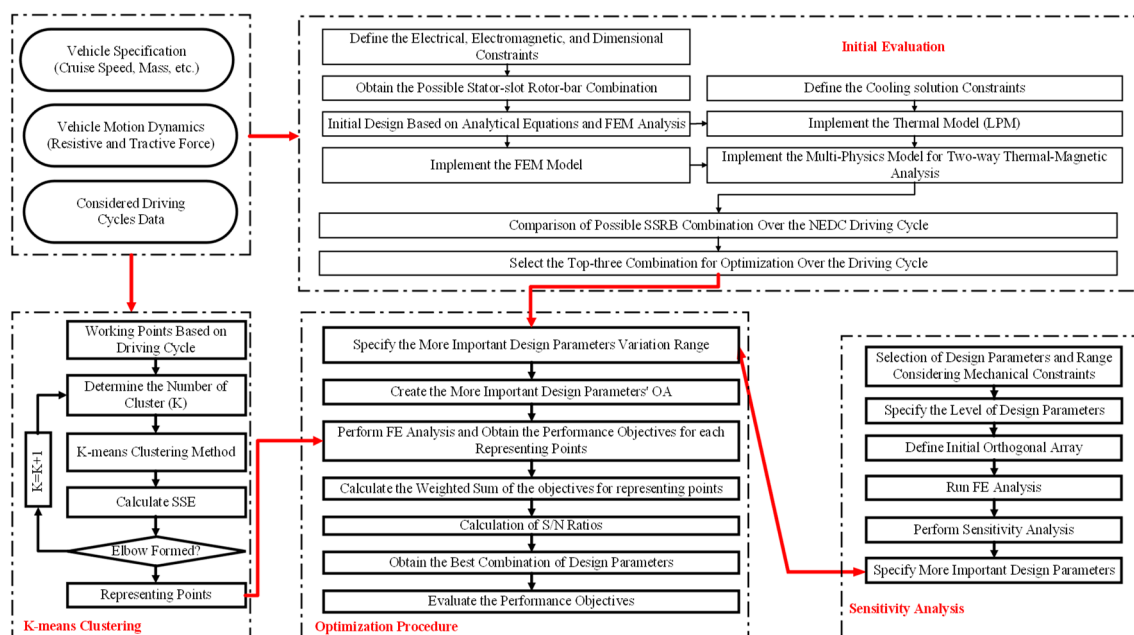


Figure 1. The proposed optimization algorithm.

### 2.1. Conceptual Design

The required envelope curve of the traction motor for EV applications should be derived based on the driving cycles, vehicle features, and dynamic equations of the vehicle. The features and expectations of the considered vehicle are presented in Table 2.

**Table 2.** The features of the considered EV.

Parameter	Value	Unit
Vehicle mass ( $M$ )	1500 kg	kg
Acceleration time ( $t_a$ )	<10 s	s
Air density ( $\rho$ )	1.225	kg/m <sup>3</sup>
Drag coefficient ( $C_D$ )	0.3	--
Rolling resistance coefficient ( $f_r$ )	0.018	--
Gearbox ratio ( $i_g$ )	13	--
Frontal area ( $A_f$ )	2.01	m <sup>2</sup>
Top speed	150	km/h
Wheel radius ( $r_d$ )	0.3	M

The dynamic behavior of the vehicle is modelled by two forces namely tractive force and resistive force. The tractive force is generated by the electric machine and acts on the wheel through the transmission system. The resistive force comprises three terms of tire rolling resistance, aerodynamic drag, and uphill resistance. According to [33], Equation (1) can be used to calculate the power required by the traction motor, discussed in detail in [33]. The overall process is to calculate the required power for drag and acceleration assuming ideal conditions. The first term in Equation (1) corresponds to the required power to accelerate the vehicle from zero speed to the base speed of  $V_b$  in  $t_a$  seconds at the slope of 0%. The second and third terms correspond to the required power for drag of the vehicle at the slope of 0%.

$$P_t = \left( \frac{\delta M}{2t_a} (V_f^2 + V_b^2) + \frac{2}{3} M g f_r V_f + \frac{1}{5} \rho C_D A_f V_f^3 \right) / \eta \quad (1)$$

$$\delta = 1 + \frac{I_w}{M r_d^2} + \frac{i_g^2 I_p}{M r^2} = 1 + \delta_1 + \delta_2 i_g^2 \quad (2)$$

where  $V_b$  is the base speed of the motor,  $\eta$  is the efficiency of the transmission system, and  $V$  is the vehicle speed. The mass correction factor ( $\delta$ ) can be calculated using Equation (2). This parameter is applied to consider the rotating inertial moment of the wheels ( $I_w$ ) and power plant ( $I_p$ ). In Equation (2), for passenger cars, the values of the  $\delta_1$  and  $\delta_2$  approximately are 0.04 and 0.0025, respectively [33].

In order to extract the motoring and generating working points of the required electric machine under four driving cycles of US06, EUDC, NEDC, and WLTP, the vehicle dynamic equations are applied, and the resultant working points are illustrated in Figure 2. Based on Equation (1) and the required working points, the parameter of  $V_b$  and required power of the electric machine will be determined. In this study, the parameters of  $V_b$  and  $P_t$  were determined to be 3800 rpm and 120 kW, respectively. In addition, to reach the top speed of 140 km/h, the maximum speed of the electric machine is set at 9000 rpm. Therefore, the required electric machine should be delivering a maximum torque of 300 N.m. until the speed of 3800 rpm is reached and, after that, working on the constant power mode until the speed of 9000 rpm is reached.

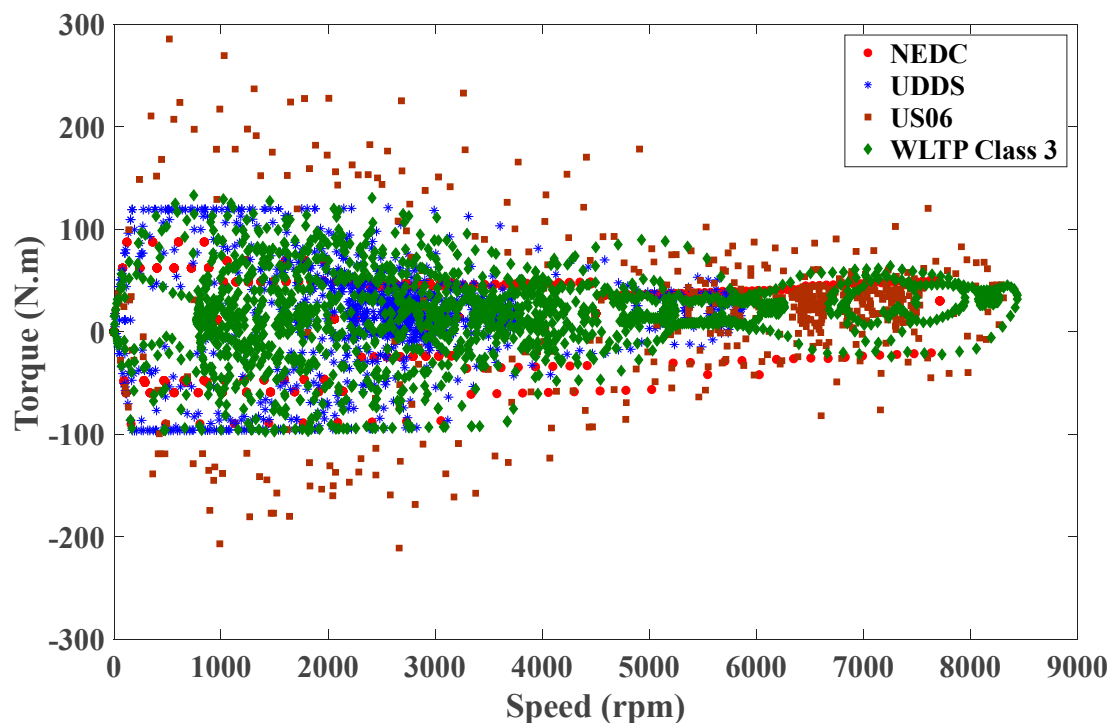


**Figure 2.** The motoring and generating working points of the required electric machine under four driving cycles of US06, EUDC, NEDC, and WLTP.

### 2.2. System Level Design Requirements

Considering the system level design of traction motors, there are some constraints regarding available space in the vehicle, the cooling system and inverter/battery constraints on current and voltage. The design constraints considered in this study are as shown in Table 3.

**Table 3.** The design constraints.

Parameter	Constraints
Stator outer diameter	$D_{os} = 260$ mm
Rotor axial length	$L = 160$ mm
Maximum current	$I_{max} = 475$ A
DC link voltage	$V_{DC}$ (peak – full battery charge) = 400 V
Cooling solution	Spiral water jacket
	Coolant: EWG50/50
	Inlet temperature = 50 °C
Fill factor	Stator coolant flow rate = Peak: 12 L/min, NEDC: 6 L/min
	50%

### 2.3. Stator and Rotor Core Material

For an informed selection of electrical steel, it is necessary to consider the working frequency and required power density. The working frequency of the motor relates to the pole number and the required maximum rotating speed. In this study, the maximum speed is 9000 rpm, and the pole number is selected as 4. Therefore, the maximum working frequency is 300 Hz, and for this working frequency, the material of M350-35A is selected.

### 2.4. Squirrel Cage Material and Manufacturing Consideration

Induction squirrel cages can be made from aluminum or copper. Aluminum is low cost and has lower environmental costs and a lower mass density (direct effect on increasing torque density). It is easier to recycle electrical machines with aluminum coils compared

to copper coils because aluminum can be recycled with steel, while recycling copper from steel is a polluting process. On the other hand, the low electrical conductivity of aluminum compared to copper may reduce its volume efficiency and increase the size of the windings and, thus, the mass of the motor. Therefore, in this study, copper is selected as the rotor cage material.

Copper cage IMs can be produced in two ways: brazing or die cast. The melting temperature of copper is above that of aluminum (1085 °C vs. 660 °C). Therefore, the use of the diecast process for copper cage IM requires very resistant and high-cost molds, which will lead to a significant increase in production costs. In addition, the above-mentioned molds will also be damaged after a period and will need to be replaced. Hence, it is more economical and conventional to use brazing. If the brazing process is selected, after welding the rotor bars to the end cage, it is necessary to stabilize the position of the rotor bars in the rotor slot by pounding. Therefore, the rotor slot must be an open slot type.

### 2.5. Electromagnetic Aspects

To minimize unbalanced magnetic forces in the radial direction, an even number of rotor bars is preferable to an odd number.

To ensure the absence of torque and current ripple associated with rotor slot harmonics, for an  $m$ -phase motor with  $p$ -pole pairs, the number of rotor bars ( $R_b$ ) for any positive integer ( $z$ ) shall be dividing  $2pmz$  or  $2p(mz \mp 1)$  as Equation (3) [34]. The range of changes in the number of rotor bars is as shown using Equation (4), where  $S_s$  is the number of stator slots,  $m$  is the number of phases,  $p$  is the pair of poles, and  $q$  is the number of slots per phase per pole.

$$R_b | 2p(mz \mp c); \forall z, c \in Z, 1 \leq z \leq 2q, -1 \leq z \leq 1 \quad (3)$$

$$p(m-1)/2 < R < 2(S_s + p) \quad (4)$$

The number of rotor bars should not be equal to the number of stator slots.

To prevent the creation of synchronous spikes, the difference between the stator slots and rotor bars should not be equal to  $2p$ ,  $4p$  and  $10p$  [35].

To limit the synchronous torques when the motor is at stall, the difference between the number of stator slots and rotor bars should not be equal to  $6p$  or any multiple of  $6p$  [36].

To prevent noise and vibration, the difference between the number of stator slots and rotor bars should not be equal to 1, 2,  $2p + 1$  and  $2p + 2$  [37].

A higher winding factor leads to a higher overload capability of the IM. The winding factor is the ratio of electromotive force produced by a stator with a short-pitch, distributed, or skewed winding, with a stator having full-pitch, concentrated, and non-skewed windings. The winding factor increases with an increase in the number of stator slots. Therefore, it is possible to eliminate the designs with winding factor less than 0.95. To calculate the winding factor, it is necessary to calculate the winding distribution coefficient ( $k_d$ ) and winding pitch coefficient ( $k_p$ ) using Equation (5).

$$k_w = k_p \cdot k_d = \frac{\sin(n\alpha/2)}{n \sin(\alpha/2)} \times \cos \frac{\gamma}{2} \quad (5)$$

where  $\alpha$  is the angle between two adjacent slots in degree,  $n$  is the number of slots per pole, and  $\gamma$  is the step shortness factor.

### 2.6. Manufacturing Aspects

There are a series of mechanical and dimensional limitations in the manufacturing process of IMs that limit the number of viable SSRB combinations: the minimum thickness of the stator teeth, the rotor bar width, and the rotor teeth width. The limit of 3 mm, based on previous experience, is considered the limit for these parameters and results in more reduction in possible SSRB combinations.

Applying the above-mentioned filters, the remaining viable SSRB combinations are mentioned in Table 4.

**Table 4.** The possible combinations of SSRB.

Number of Stator Slot	Number of Rotor Bar
$S_s = 48$	$R_b = (58, 62, 66, 70, 74, 78, 82)$
$S_s = 60$	$R_b = (70, 74, 78, 82)$
$S_s = 72$	$R_b = 82$

### 3. Initial Design

By applying the mentioned filters, the number of available combinations has been greatly reduced. Now, to obtain the best possible combination, it is necessary to design 12 machines with the indicated SSRB combinations and compare their performance over an entire driving cycle. For initial designs, the conventional analytical design procedure is utilized and then the initial design is modified using finite element modelling (FEM).

For EV traction motors, the specific electrical and magnetic loading can assume water-cooling. The outer diameter and axial length of the machine are constrained by available space and overall mass restriction. Therefore, 12 IMs with a maximum power of 120 kW at 3800 rpm are analytically designed with the same outer stator diameter and axial length.

#### 3.1. Cooling Solution and Thermal Analysis Model

To accurately extract the traction capability curve of the current traction motor, it is necessary to perform multi-physics electromagnetic–thermal analysis. Power density is limited by two factors: the maximum current density in the coils and the maximum flux density. While the maximum flux density is related to the magnetic properties of the material, the maximum allowable current of the windings is limited by the cooling system and insulation class. Therefore, the cooling system plays an important role and is a decisive factor in reducing the temperature or from another point of view; it allows an increase in the maximum current density at a constant winding temperature. Therefore, accurate and appropriate analysis of temperature distribution in different parts of the electric machine is important.

Like electromagnetic analysis, thermal analysis can be divided into two main categories of analytical and numerical methods. The advantages of analytical methods are less complexity and acceptable accuracy, especially in the initial design step. In this paper, the analytical model of lumped parameter model (LPM) is considered for thermal analysis. In the LPM, the electric motor parts modelled as a heat storage source and heat source (losses of the electric motor). These sources then connected to each other through the geometry dependent thermal resistances, which depended on the geometry of the motor and material characteristics [38,39]. The details of the considered LPM model of water-cooled IM are shown in Figure 3.

#### 3.2. Driving Cycle Performance Evaluation

The performance of the designed motor has been compared in the NEDC driving cycle in terms of three performance indexes: consumed energy, average winding temperature and average input current. The reason for choosing these three parameters are as follows.

##### 3.2.1. Consumed Energy ( $E$ )

One of the important parameters in examining the performance of an EV is the amount of consumed energy per 100 km, expressed as kWh/100 km. To calculate the consumed energy, it is necessary to accurately calculate the losses and efficiency of the IM over the driving cycle. Analytical methods for measuring core losses and copper losses do not have

proper accuracy, so it is necessary to use the FEM method to calculate losses. Accurate prediction of core loss is carried out using Equation (6).

$$P_{core} = k_h f B_m^n + k_e f^2 B_m^2 + k_a f^{1.5} B_m^{1.5} \quad (6)$$

where  $k_h$ ,  $k_e$  and  $k_a$  are coefficients of hysteresis, eddy current and additional losses, respectively.  $f$  is the electric frequency and  $B_m$  is the amplitude of the magnetic flux density.

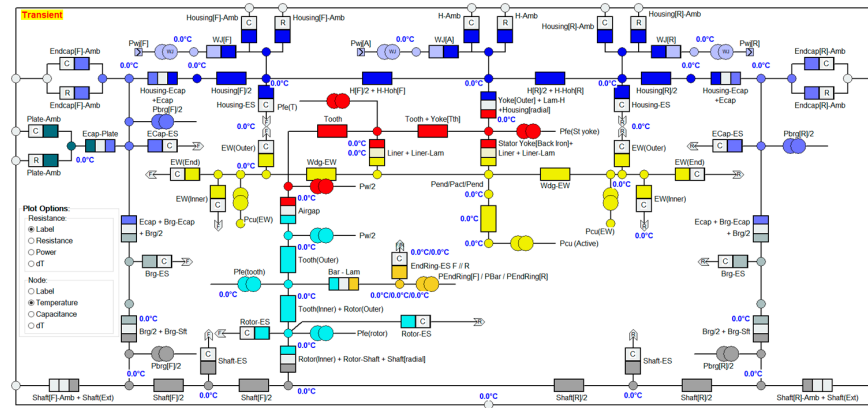


Figure 3. The LPM model of IM.

In relation to the losses of the stator winding, in addition to DC losses of the winding, the skin and proximity effects must be considered. In the AC excitation, the high-frequency current tends to flow through the surface of the conducting material and consequently the effective cross-sectional area of the conducting material will reduce. This phenomenon, known as the skin effect, results in a higher resistance and consequently higher copper losses. Additionally, when an alternating current (AC) flows through a conductor, it creates an associated alternating magnetic field around it. The alternating magnetic field induces eddy currents in adjacent conductors, altering the overall distribution of current flowing through them. This phenomenon is known as the proximity effect. The proximity effect can significantly increase the AC resistance of adjacent conductors. Therefore, the overall copper losses of the motor are calculated using Equation (7).

$$P_{copper} = P_{copper}^{AC} + P_{copper}^{DC} \quad (7)$$

Consumed energy over the NEDC driving cycle can be calculated using Equation (8). It should be noted that in the performance comparison, the mechanical losses are not considered as they will not vary for different SSRB combinations.

$$E = \int_{t=1}^{t=1180} P_{in,motoring}(t) \cdot dt - \int_{t=1}^{t=1180} P_{out,generating}(t) \cdot dt \quad (8)$$

### 3.2.2. The Average Temperature of the Coils ( $T_{ave}$ )

A lower working winding temperature will give a higher expected lifetime of the insulation and consequently improve the electric motor life cycle. Increasing the working temperature also leads to an increase in the winding resistance and consequently lower efficiency. Therefore, it is better to have a lower average working temperature. To accurately calculate the average working temperature of the winding, the coupled electromagnetic-thermal analysis is carried out for 10 continuous NEDC driving cycles.

### 3.2.3. Average Input Current ( $I_{ave}$ )

The lifetime of lithium batteries used in EV applications directly corresponds to the discharge current, with a lower discharge current giving a longer lifetime. Therefore, this

parameter is considered as the third performance index. Average input current also takes account of the operating power factor, therefore ensuring the influence of SSRB combination on power factor is included in the objective function.

To obtain the optimal combinations, the weighted sum approach is utilized as Equation (9). In Equation (9), the values of  $\omega_1$ ,  $\omega_2$  and  $\omega_3$  are equal to 0.6, 0.2, and 0.2, respectively. It should be noted that the values of Equation (9) are normalized using Equation (10).

$$F(x) = \omega_1 E(\text{Normalized}_i) + \omega_2 I_{ave}(\text{Normalized}_i) + \omega_3 T_{ave}(\text{Normalized}_i) \quad (9)$$

$$F(\text{Normalized}_i) = \frac{f(i) - \min(x)}{\max(x) - \min(x)} \quad (10)$$

The normalized values of the objective functions ( $E_n$ ,  $I_{ave,n}$ , and  $T_{ave,n}$ ) are presented in Table 5. These data are used to calculate the overall objective functions of  $F(x)$ . The combination with the lowest  $F(x)$  means a lower consumed energy, lower input current, and lower working temperature and is considered as the optimum design. Therefore, based on Table 5, the best three combinations of S48R58, S48R62 and S60R74 are selected as optimum combinations and will be considered for optimization over the driving cycle and further studies. The winding configuration of these SSRB combinations are presented in Appendix A. The average working temperature of these optimum combinations over five driving cycles of NEDC is illustrated in Figure 4.

**Table 5.** Comparison of different SSRB combinations in the NEDC driving cycle.

Combination	$E(\text{kWh})$	$I_{ave}(\text{A})$	$T_{ave}$	$E_n(\text{kWh})$	$I_{ave,n}(\text{A})$	$T_{ave,n}$	$F(x)$
S48R58 (Audi e-Tron)	1.353	55.29	55.28	0.079	0	0	0.047
S48R62	1.338	55.43	55.44	0	0.002	0.009	0.002
S48R66	1.511	93.088	68.36	0.915	0.802	0.774	0.864
S48R70 (Tesla Front Motor)	1.524	95.77	69.54	0.984	0.859	0.844	0.931
S48R74	1.505	94.39	68.46	0.883	0.830	0.780	0.852
S48R78	1.513	94.36	68.85	0.925	0.829	0.803	0.882
S48R82	1.516	93.2	68.71	0.941	0.805	0.795	0.885
S60R70	1.46	102.38	64.44	0.645	1	0.542	0.695
S60R74 (Tesla Rare Motor)	1.361	68.15	56.14	0.121	0.273	0.050	0.137
S60R78	1.472	101.8	64.98	0.708	0.987	0.574	0.737
S60R82	1.474	100.35	72.16	0.719	0.956	1	0.823
S72R82	1.527	89.36	71.32	1	0.723	0.950	0.934

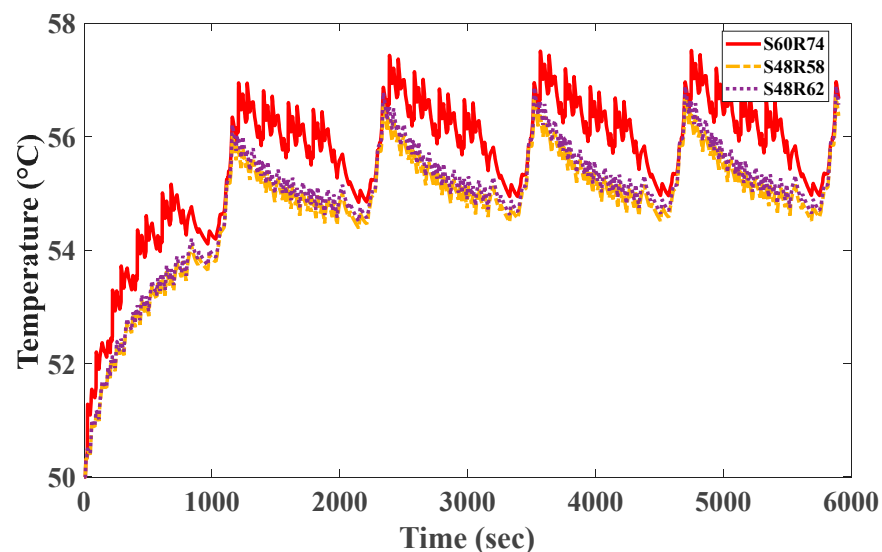


**Figure 4.** Winding temperature changes in 5 NEDC duty cycles.

#### 4. Optimization over Driving Cycle

A large portion of consumed energy in electric vehicles is related to traction. Therefore, it is necessary to optimize the IM to increase efficiency and consequently increase the range of the vehicle. The aim of this section is to reconcile the highest performance working region of the designed IM with the part of the speed–torque curve where the most operating points are located. This results in increased vehicle mileage, lower energy consumption, and higher overall energy efficiency. Therefore, three objective functions of efficiency, power factor, and rotor losses are considered as objective functions. The rotor losses are considered to avoid the need for mandatory rotor cooling.

##### 4.1. Calculation of the Representing Points

In this paper, the K-means clustering method is utilized to obtain the representing points of the designed IM over four driving cycles of NEDC, US06, WLTP Class 3, and EUDC. Clustering  $j$  observations of  $(x_1, x_2, \dots, x_j)$ , whole operating points of the machine, into  $k \leq j$  sets  $S = \{S_1, S_2, \dots, S_k\}$ , representing points, is the aim of the K-means algorithm. In this method, the target is to minimize the variance of each cluster. The exact mathematical definition is stated as Equation (11).

$$\operatorname{argmin}_S \sum_{i=1}^k \sum_{x \in S_i} \|x - \mu_i\|^2 = \operatorname{argmin}_S \sum_{i=1}^k |S_i| \operatorname{Var}(S_i) \quad (11)$$

where  $\mu_i$  is the mean of the points in  $S_i$ . This is equivalent to minimizing squares of deviations from points in the same cluster.

To obtain the optimum number of clusters (representing points), the elbow method is utilized. To implement the elbow method, the distortion criterion is computed as the sum of the squares of the distances between each cluster's center and its data. By calculating and plotting this criterion for different cluster numbers, the optimum cluster number can be selected. As shown in Figure 5a, the optimum cluster number is 6. Therefore, using the k-means method with the optimum cluster number of 6, the representing points of the designed motor over considered driving cycle are calculated as shown in Figure 5b. The details of these representing points are presented in Table 6.

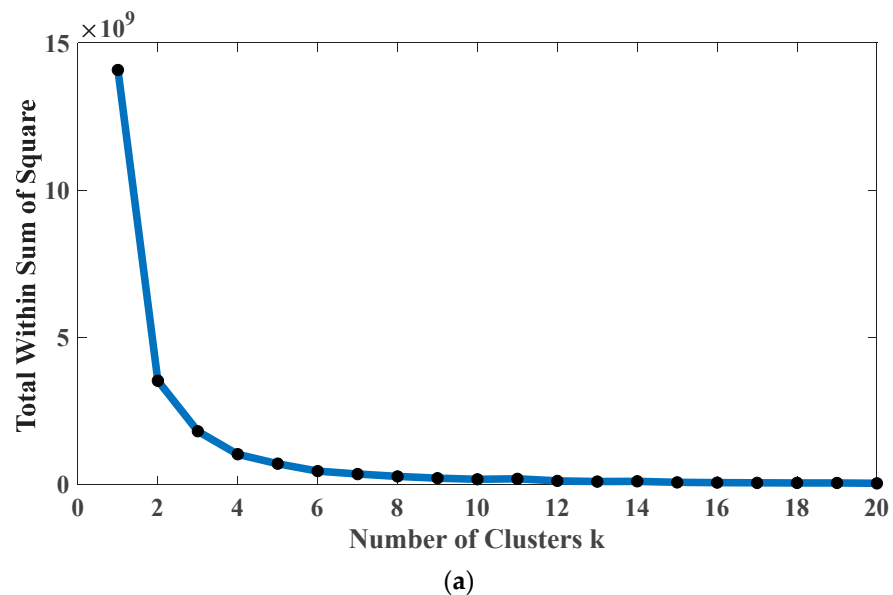
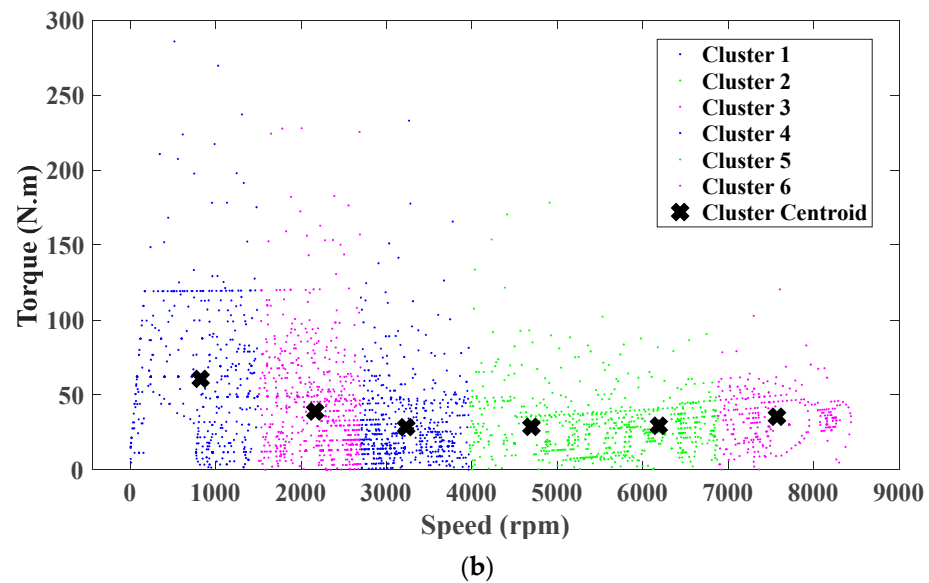


Figure 5. Cont.



**Figure 5.** The calculated representative points of the k-means clustering method. (a) The effect of the number of clusters on the sum of the deviation squares; (b) the calculated clustering points.

**Table 6.** Equivalent points obtained from the k-means method.

Cluster	Speed (rpm)	Power (kW)	Torque (N·m)	Weight
1	3178	9251.8	27.8	861
2	7848	28847	35.1	354
3	800	4909.3	58.6	623
4	4579	13187	27.5	525
5	2118	8051.2	36.3	980
6	6095	19276	30.2	489

#### 4.2. Sensitivity Analysis

There are a lot of design parameters that can be determined and optimized in the design process of electrical machines. Optimizing all these parameters will result in high computational time and memory required. Some of these parameters do not have a significant impact on the overall performance of the electric machine and just complex the design optimization process. Therefore, it is necessary to use some methods to specify these parameters and eliminate them in the optimization procedure. For this purpose, it is necessary to use the sensitivity analysis (SA) method to specify the more important design parameters. The available methods to perform SA are local SA, global SA, analysis of variance, correlation coefficients, and signal-to-noise (S/N) ratio [40]. In this paper, the S/N ratio, which is based on Design of Experiment (DOE), is utilized. The DOE approach is based on predefined tables known as orthogonal arrays (OAs). In the OAs, columns of the arrays are balanced and orthogonal. This means that in each pair of columns, all factor combinations occur the same number of times [41]. OA designs estimate the effect of each factor on the objectives independently of all other factors.

In the optimization process of IMs, there are a lot of design parameters and applying a single-stage SA is not efficient, so it is better to use two-stage SA. Therefore, the SA is performed separately for stator and rotor parameters.

##### 4.2.1. Rotor Parameters

For SA of the rotor geometric parameters, six parameters: airgap, bar opening width ( $B_{r0}$ ), bar opening radius ( $B_{r1}$ ), end ring width ( $H_e$ ), bar opening depth ( $H_{r01}$ ), and bar depth ( $H_{r2}$ ), are considered. The considered levels of the rotor parameters for different SSRB combinations are presented in Table 7.

**Table 7.** Rotor design parameters and considered levels.

Combination	Level	Airgap	B <sub>r0</sub>	B <sub>r1</sub>	H <sub>e</sub>	H <sub>r01</sub>	H <sub>r2</sub>
S48R58	1	0.45	0.9	1.53	18	0.54	18
	2	0.5	1	1.7	20	0.6	20
	3	0.55	1.1	1.87	22	0.66	22
S48R62	1	0.45	0.9	1.35	18	0.54	18
	2	0.5	1	1.5	20	0.6	20
	3	0.55	1.1	1.65	22	0.66	22
S60R74	1	0.45	0.9	1.17	18	0.54	20
	2	0.5	1	1.3	20	0.6	22
	3	0.55	1.1	1.43	22	0.66	24

For 6 parameters and 3 levels, the utilized OA is L<sub>27</sub>(3<sup>6</sup>), where 27 is the number of required FEM samples. The S/N ratio for an experiment is calculated based on different optimization goals. The optimization goal is minimizing Equation (9). Therefore, the utilized equation for minimization is Equation (12).

$$S/N = -10 \log \left( \sum_{i=1}^n \frac{y_i^2}{v} \right) \quad (12)$$

where  $v$  is the number of repeats in each experiment and  $y_i$  is the output of the experiment in  $i$ -th repeat. Based on the calculated S/N ratio, the importance degree of each design parameter is specified. The results of S/N analysis are shown in Table 8. According to the obtained results, in all three designs, parameters B<sub>r1</sub>, B<sub>r0</sub> and H<sub>r2</sub> are more important design parameters.

**Table 8.** Importance of rotor parameters for different combinations.

	Combination	Airgap	B <sub>r0</sub>	B <sub>r1</sub>	H <sub>e</sub>	H <sub>r01</sub>	H <sub>r2</sub>
Rank	S48R58	5	3	1	4	6	2
	S48R62	5	3	1	4	6	2
	S60R74	5	3	1	4	6	2

#### 4.2.2. Stator Parameters

Six design parameters: slot opening width (B<sub>s0</sub>), slot opening depth (H<sub>s0</sub>), slot opening depth (H<sub>s1</sub>), slot depth (H<sub>s2</sub>), slot bottom radius (R<sub>s</sub>), and tooth width (T<sub>w</sub>), are considered. The considered levels of the stator parameters for different SSRB combinations are presented in Table 9.

**Table 9.** Stator design parameters and considered levels.

Combination	Level	B <sub>s0</sub>	H <sub>s0</sub>	H <sub>s1</sub>	H <sub>s2</sub>	R <sub>s</sub>	T <sub>w</sub>
S48R58	1	2.25	0.9	0.9	18	0.9	3.6
	2	2.5	1	1	20	1	4
	3	2.75	1.1	1.1	22	1.1	4.4
S48R62	1	2.25	0.9	0.9	18	0.9	3.6
	2	2.5	1	1	20	1	4
	3	2.75	1.1	1.1	22	1.1	4.4
S60R74	1	2.25	0.9	0.9	18	0.9	3.24
	2	2.5	1	1	20	1	3.6
	3	2.75	1.1	1.1	22	1.1	3.96

The same SA procedure is utilized for stator parameters and the results of SA are presented in Table 10. According to the obtained results, for S60R74 combination, three parameters,  $T_w$ ,  $H_{s0}$  and  $B_{s0}$ , are more important, while for S48R58 and S48R62 combinations, the parameters of  $T_w$ ,  $B_{s0}$  and  $H_{s2}$  are more important.

**Table 10.** Importance of stator parameters for different combinations.

	Combination	$B_{s0}$	$H_{s0}$	$H_{s1}$	$H_{s2}$	$R_s$	$T_w$
Rank	S48R58	2	4	5	3	6	1
	S48R62	2	4	5	3	6	1
	S60R74	3	2	5	4	6	1

Finally, the six most important design parameters of each SSRB combination are presented in Table 11.

**Table 11.** More important design parameters.

Combination	Rotor			Stator		
S48R58	$Br_1$	$Hr_2$	$Br_0$	$T_w$	$B_{s0}$	$H_{s2}$
S48R62	$Br_1$	$Hr_2$	$Br_0$	$T_w$	$B_{s0}$	$H_{s2}$
S60R74	$Br_1$	$Hr_2$	$Br_0$	$T_w$	$B_{s0}$	$H_{s0}$

#### 4.3. Taguchi Optimization Method

By considering five levels for each of the specified important design parameters, the predefined OA of  $L_{25}(6^5)$  is considered for optimization. Where 25 is equal to the number of required simulations for each representative point. The considered levels for design parameters are shown in Table 12.

**Table 12.** Considered levels of design parameters.

Parameters	Level	1	2	3	4	5
General	$B_{r0}$	0.5	0.675	0.85	1.025	1.2
	$T_w$	3.5	3.75	4	4.25	4.5
	$B_{s0}$	1.5	1.875	2.25	2.625	3
S48R58	$Br_1$	1.4	1.5	1.6	1.7	1.8
	$Hr_2$	18	19	20	21	22
	$H_{s2}$	18	19	20	21	22
S48R62	$Br_1$	1.3	1.4	1.5	1.6	1.7
	$Hr_2$	19	20	21	22	23
	$H_{s2}$	18	19	20	21	22
S60R74	$Br_1$	1.2	1.3	1.4	1.5	1.6
	$Hr_2$	21	22	23	24	25
	$H_{s0}$	0.5	0.675	0.85	1.025	1.2

For each SSRB combination, the objective functions of efficiency ( $Eff$ ), power factor ( $Pf$ ) and rotor ohmic losses ( $P_{loss,r}$ ) are calculated for six calculated representative points. In the optimization process, the weighted sum approach is utilized to convert the multi-objective optimization problem to a single objective optimization problem. The utilized formula is as follows:

$$f(i) = \frac{\sum_{k=1}^{k=6} w_k Eff(i, k) \times Pf(i, k)}{P_{loss,r}(i, k)} \tag{13}$$

where  $Eff(i, k)$ ,  $Pf(i, k)$  and  $P_{loss,r}(i, k)$  are the normalized terms of the objective functions. The values of the calculated F(T) are presented in Table 13.

**Table 13.** The considered OA and calculated objective functions.

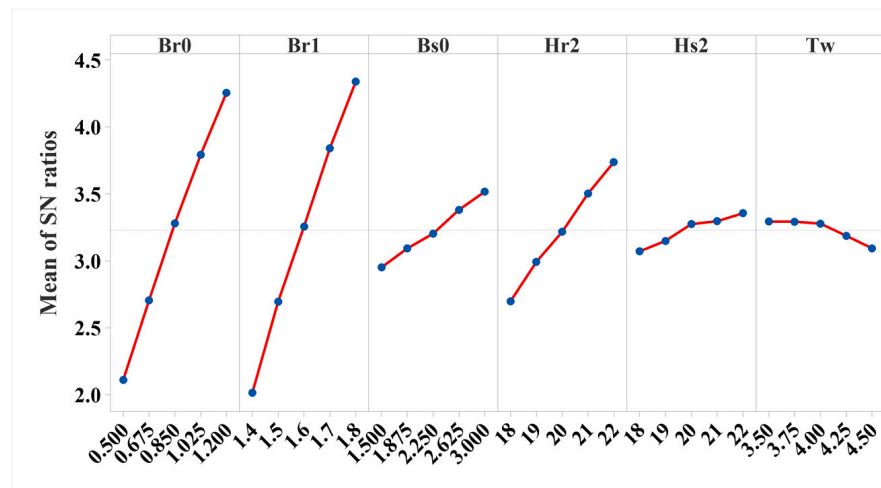
Run	B <sub>r0</sub>	B <sub>r1</sub>	B <sub>s0</sub>	H <sub>r2</sub>	H <sub>s2</sub> or H <sub>s0</sub>	T <sub>w</sub>	F(S48R58)	F(S48R62)	F(S60R74)
1	1	1	1	1	1	1	0.999571	1	1
2	1	2	2	2	2	2	1.14672	1.178643075	1.120145392
3	1	3	3	3	3	3	1.287534	1.343249221	1.228997026
4	1	4	4	4	4	4	1.441112	1.523293328	1.346431587
5	1	5	5	5	5	5	1.58606	1.689944819	1.459677922
6	2	1	2	3	4	5	1.157999	1.182201304	1.054392338
7	2	2	3	4	5	1	1.350724	1.429960442	1.288456405
8	2	3	4	5	1	2	1.461752	1.550894444	1.439874009
9	2	4	5	1	2	3	1.419667	1.545910033	1.385474052
10	2	5	1	2	3	4	1.462875	1.519391356	1.420247376
11	3	1	3	5	2	4	1.322145	1.380053217	1.256382628
12	3	2	4	1	3	5	1.300039	1.39815585	1.224421689
13	3	3	5	2	4	1	1.494479	1.641514633	1.45478308
14	3	4	1	3	5	2	1.547381	1.632967242	1.495550909
15	3	5	2	4	1	3	1.662775	1.763532382	1.672829335
16	4	1	4	2	5	3	1.359613	1.472702751	1.294748672
17	4	2	5	3	1	4	1.467932	1.589391726	1.423886911
18	4	3	1	4	2	5	1.513388	1.566579393	1.464160797
19	4	4	2	5	3	1	1.755273	1.887332662	1.744978671
20	4	5	3	1	4	2	1.674067	1.843693819	1.651972402
21	5	1	5	4	3	2	1.532637	1.672632372	1.491201914
22	5	2	1	5	4	3	1.597424	1.682090225	1.539115958
23	5	3	2	1	5	4	1.531169	1.659756142	1.459835445
24	5	4	3	2	1	5	1.642692	1.778602992	1.61837731
25	5	5	4	3	2	1	1.881142	2.084129635	1.888590242

Using the Taguchi method and values of S/N ratio, the optimal combination of design parameters can be obtained. The obtained results of different combinations are shown in Figure 6. For example, the optimum levels of design parameters corresponded to highest S/N value for S48R58 are  $B_{r0}$  (level 5 = 1.2),  $B_{r1}$  (Level 5 = 1.8),  $B_{s0}$  (level 5 = 3),  $H_{r2}$  (Level 5 = 22),  $H_{s2}$  (Level 5 = 22), and  $T_w$  (level 1 = 3.5). The optimal combination of design parameters for all three designs are presented in Table 14.

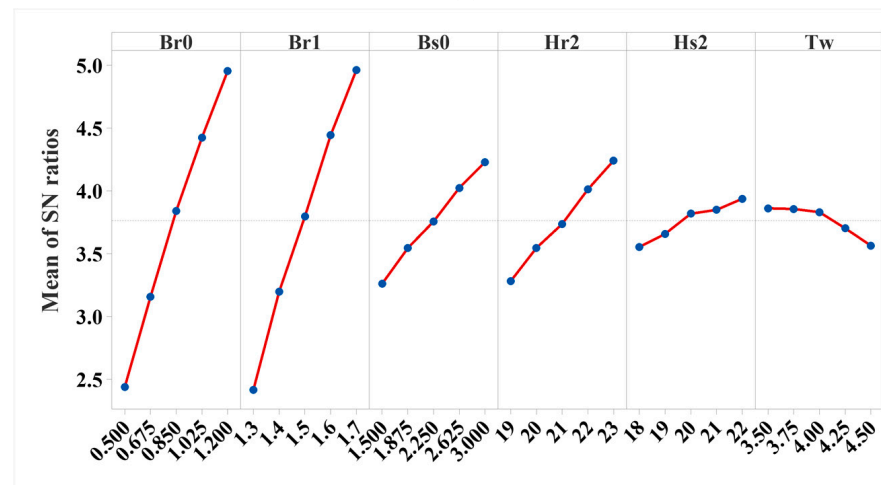
**Table 14.** The optimal combination of design parameters.

Parameter	B <sub>r0</sub>	T <sub>w</sub>	H <sub>s2</sub>	H <sub>r2</sub>	B <sub>s0</sub>	B <sub>r1</sub>	H <sub>s0</sub>
S48R58	1.2	3.5	22	23	3	1.7	*
S48R62	1.2	3.5	22	22	3	1.8	*
S60R74	0.5	4.5	*	21	1.675	1.2	0.5

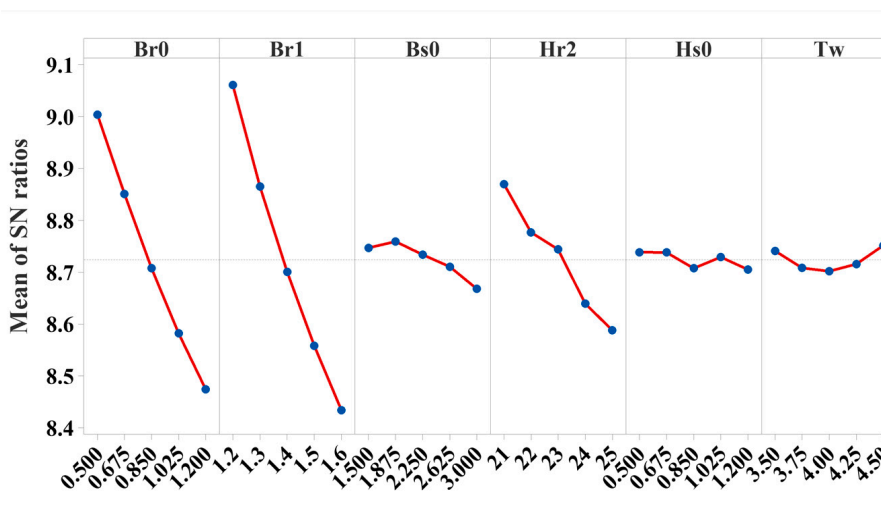
\* means that this parameter is not valid for this SSRB combination.



(a)



(b)



(c)

Figure 6. The results of the S/N ratio: (a) S48R58, (b) S48R62, and (c) S60R74.

## 5. Evaluation

The performance of the optimum designs is compared in terms of robustness against manufacturing tolerances, magnetic flux density distribution, mechanical stress analysis, nominal envelope curve, and efficiency map to select the best SSRB combinations.

### 5.1. Robustness against Manufacturing Tolerances and Noise Factors

According to the results shown in Figure 6, for all three combinations, the values of S/N ratio are positive, indicating that the effect of manufacturing tolerances on the objective is less. A higher S/N ratio indicates a high tolerability against manufacturing tolerances. Therefore, the S60R74 are more tolerant to manufacturing tolerances and unwanted noise factors followed by S48R62 and S48R58, respectively.

### 5.2. Magnetic Flux Density Distribution

The magnetic flux density distribution of the optimum designs is illustrated in Figure 7. The considered working point is 120 kW at 3800 rpm and DC voltage of 400 V. According to the obtained results, it is obvious that the stator and rotor tooth of the S48R58 combination is more saturated compared to S48R62 and S60R74 combinations. Between S48R62 and S60R74, the latter has slightly better characteristics.

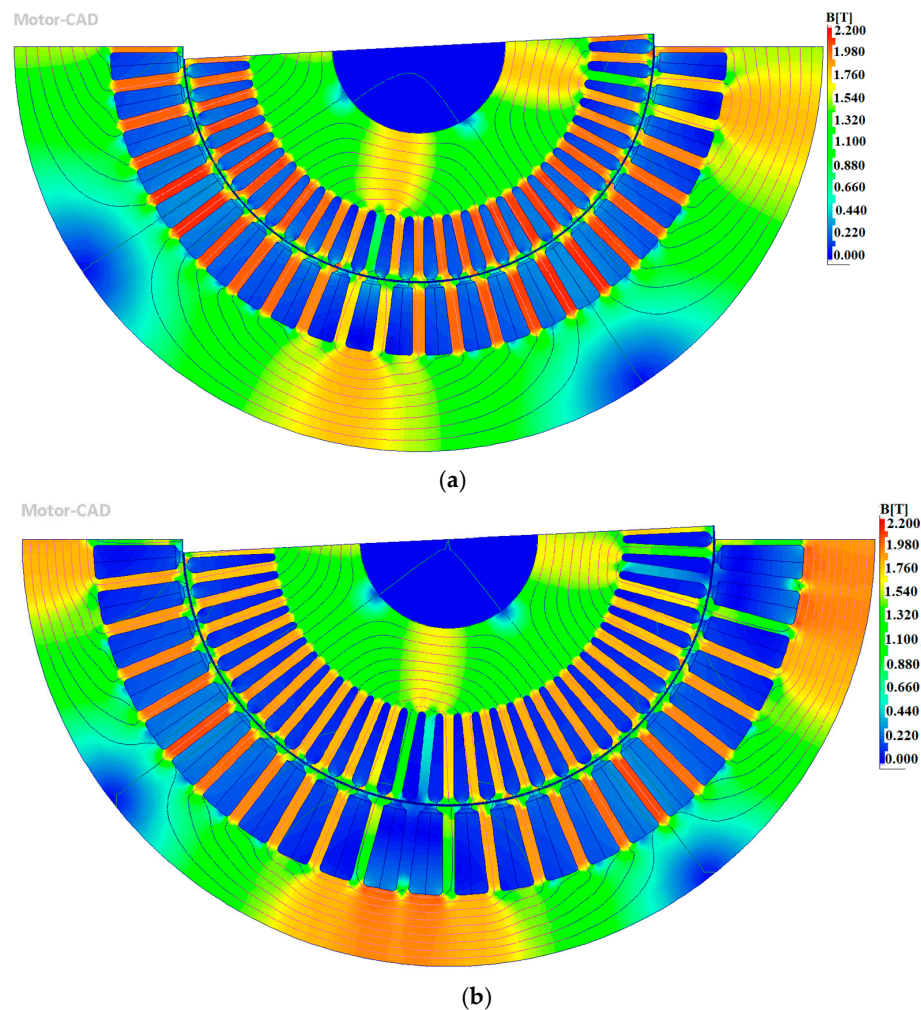
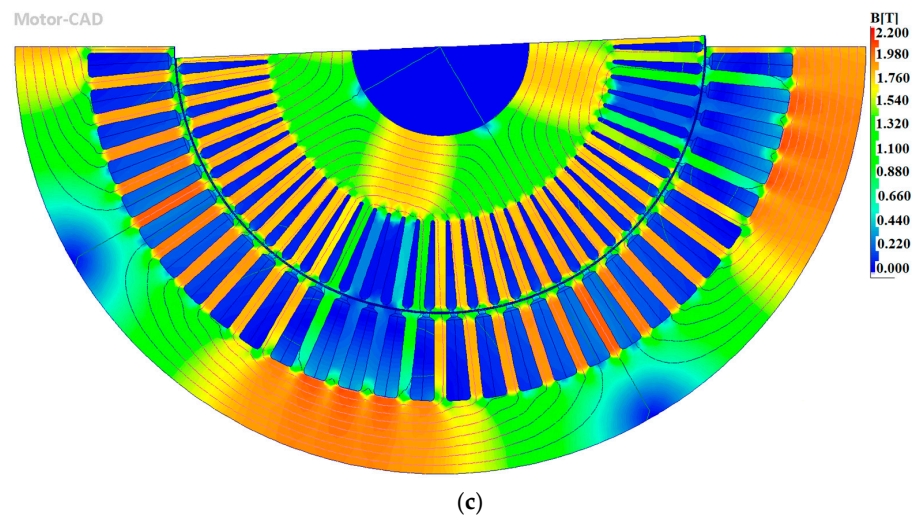


Figure 7. Cont.



**Figure 7.** The magnetic flux density of the optimum designs: (a) S48R58, (b) S48R62, and (c) S60R74.

### 5.3. Mechanical Stress Analysis

The steady-state performance of the designed IMs is investigated using static structural FE. For this purpose, the Von Mises stress (VMS) due to centrifugal force is used to evaluate the mechanical tolerability. It should be noted that there are some additional loads that are caused by vibration, thermal expansion, rotor dynamic, and electromagnetic forces. But since they have little impact on the overall applied stress, they are disregarded. In the static structural FE analysis, there is some degree of uncertainty, and it is recommended that a factor of safety (FoS) should be considered. Due to the severe loading condition and harsh environment of the EV applications, this parameter is considered as 2. The maximum working speed of this traction motor is 9000 rpm but, according to the standard, traction motors should function correctly at 20% higher speed. Therefore, the mechanical analysis is carried out at 10,800 rpm. The yield strength of M250-35A is  $455 \text{ N/mm}^2$ . With an FoS of 2, the limitation of applied VMS is  $227.5 \text{ N/mm}^2$ . As shown in Figure 8, the obtained results indicate that all three designs have a proper condition and there is no risk of mechanical failure. However, the S48R58 and S48R62 combinations have a slightly better performance.

### 5.4. Nominal Envelope Curve Considering Thermal Aspects

In EVs, generally, a temperature sensor is installed at the hotspot point of the winding to protect the motor against overheating. The considered temperature value for this point is based on the designer's opinion and expected lifetime or overhaul time of the traction motor. Therefore, based on capabilities of the utilized traction motor, it is possible to consider a lower temperature for the hotspot limit.

To evaluate the envelope curves of the optimum designs, two-way electromagnetic thermal analysis with consideration of limited hotspot temperature is carried out. It should be noted that in multi-physics analysis the following parameters are considered.

1. The winding's hotspot temperature is  $155 \text{ }^\circ\text{C}$  (the considered insulation class of the winding is class H with a corresponding temperature of  $180 \text{ }^\circ\text{C}$ ; however, due to ignoring some parameters like drive harmonics, etc., the lower temperature threshold is considered);
2. The switching type is sine/triangle with third harmonic injection;
3. The corresponding DC link voltage to the selected switching method is  $400 \text{ V}$ ;
4. The maximum current limit is  $475 \text{ A}$ .

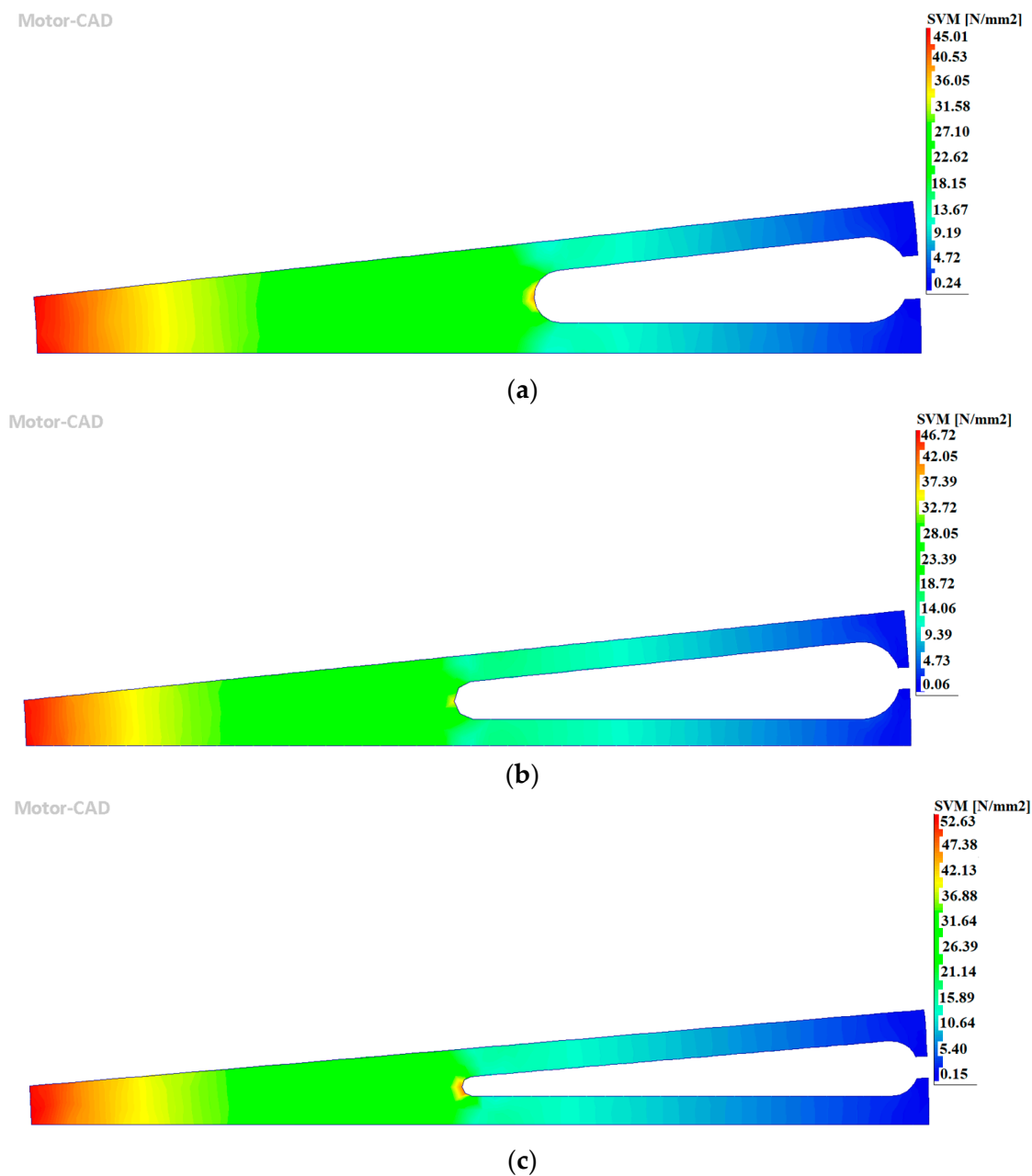


**Figure 8.** The Von Mises (equivalent) stress of the rotor at speed of 9000 rpm: (a) S48R58, (b) S48R62, and (c) S60R74.

The obtained results of Figure 9 indicate that for speeds lower than the base speed of 3800 rpm (base speed), the S60R74 combination can deliver higher torque followed by S48R62 and S48R58 combinations.

For speeds higher than 3800 rpm, the nominal power of the S48R62 and S60R74 combinations is about 70 kW, while this value for S48R48 parameters is about 64 kW. The S48R62 combination can effectively deliver 70 kW until 9000 rpm, whereas the nominal power of S60R74 combination is slightly reduced at higher speed. In other words, the S48R62 combinations have a wider constant power speed region.

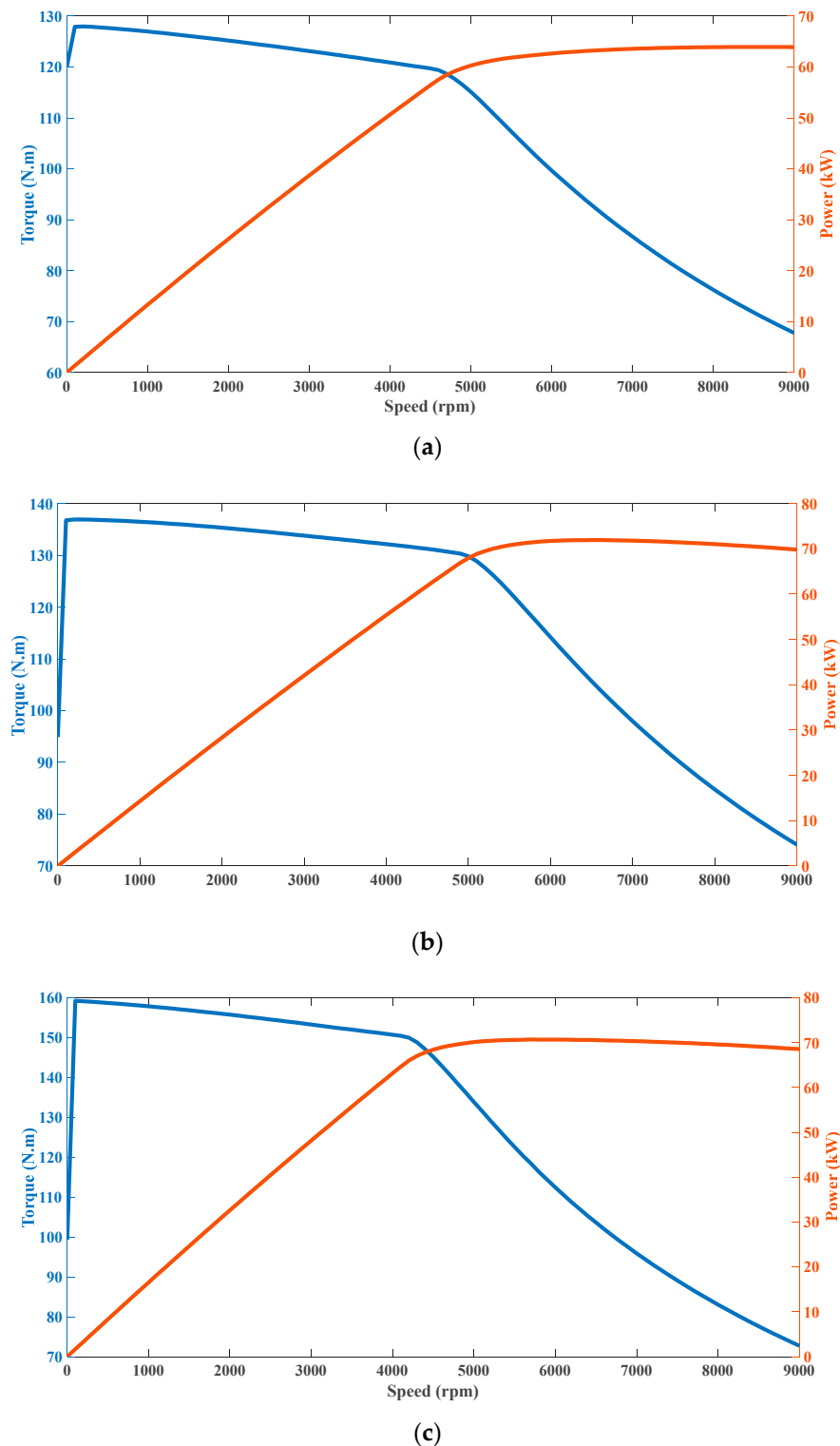
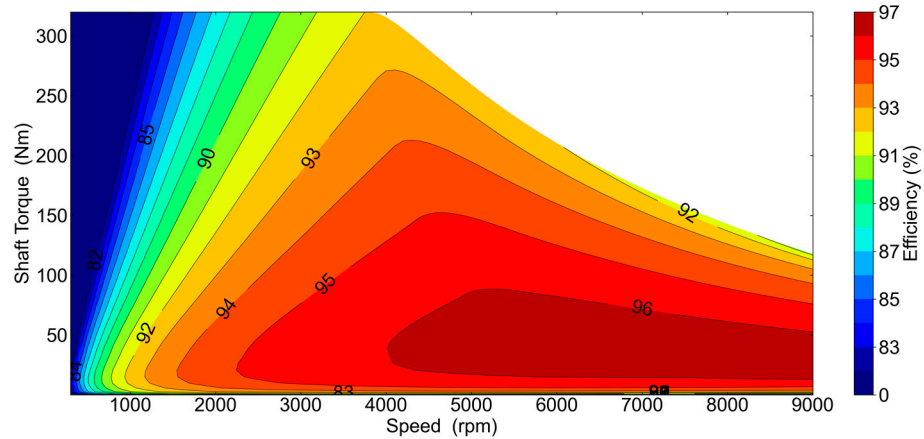


**Figure 9.** The nominal envelope curve of the optimum designs: (a) S48R58, (b) S48R62, and (c) S60R74.

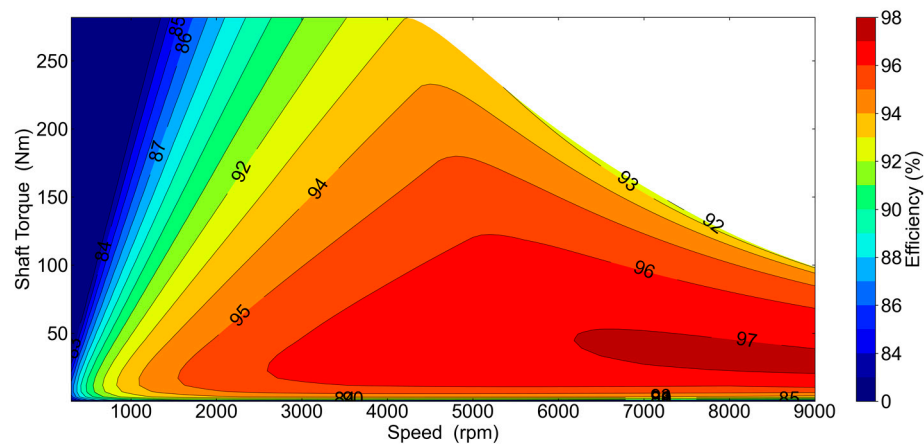
### 5.5. Efficiency Map

The efficiency maps of the optimum designs are illustrated in Figure 10. In the calculation process, the maximum current is set to 475A, and the DC link voltage is 400 V with a maximum modulation index of 1. It is obvious that the S48R48 and S60R74 can properly deliver the required torque of 300 N.m, whereas for S48R62 combination, the maximum torque is limited to 270 N.m. The wider high-efficiency region results in better performance in the driving cycle and implies an improved vehicle range. The S48R62 has a

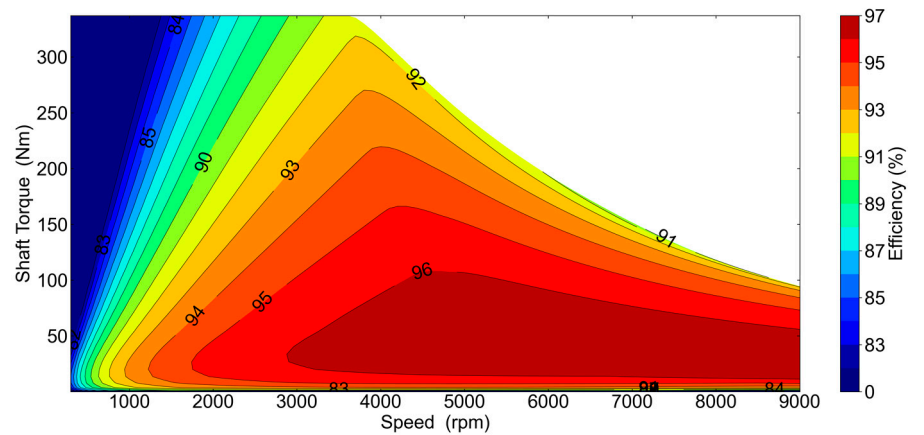
region with maximum efficiency of 97%, while for the other two, it is limited to 96%. For regions with an efficiency over 96%, the S48R62 and S60R74 have wider higher efficiency regions compared to S48R58. For example, in the S48R58 design the optimum region starts from a speed of around 4000 rpm and the torque is lower than 90 N.m. For S48R62 and S60R74, it starts from 3000 rpm and its torque value is higher than 100 N.m.



(a)



(b)



(c)

Figure 10. The efficiency maps of the optimum designs: (a) S48R58, (b) S48R62, and (c) S60R74.

The S48R62 combination could not provide the transient requirements, and its maximum torque is below 300 N.m. Therefore, despite its superior performance over the driving cycle, the improved efficiency and nominal torque envelope, it is not selected as an optimum design. Between S48R58 and S60R74, the latter one has a wider high efficiency region and has better performance. Therefore, the S60R74 combination is selected as the optimum design.

## 6. Conclusions

In this paper, a sequential Taguchi method for design optimization of IM by considering driving cycle performance was introduced. The case study was a 120 kW water-cooled copper cage IM.

In the proposed systematic design, the number of possible and applicable SSRB combinations is reduced. First, based on a series of empirical and mathematical relationships, the available options are specified. Then, the remaining optimum SSRB combinations are optimized over the four driving cycles of NEDC, US06, WLTP Class 3, and EUDC using representative points calculated using K-means clustering. The proposed design optimization procedure requires a minimum number of FEM results and effectively reduced the required time for optimization. By comparison of different SSRB combinations, it was found that the S60R74 had a superior performance compared to other designs and was selected as an optimum design. The proposed method requires the minimum number of FEM samples and can efficiently optimize the IM over driving cycles.

It was found that the S48R62, which had the highest efficiency region (over 97%), could not deliver the required torque envelope. It is therefore shown that the K-means clustering method is not completely robust for the design of electric machines for electric vehicle traction motors. The method focuses on regions with high-density working points, and it is necessary to add the envelope curve and transient operation mode to existing clustering or representative point calculation methods for robust analysis.

**Author Contributions:** Methodology, F.M.; Software, F.M.; Writing—original draft, F.M.; Writing—review & editing, N.J.B. All authors have read and agreed to the published version of the manuscript.

**Funding:** This research was funded by UKRI under Innovate UK grant 10011291.

**Data Availability Statement:** The data presented in this study are available on request from the corresponding author.

**Conflicts of Interest:** The authors declare no conflict of interest.

## Symbols and Abbreviations

EV	Electric Vehicle
SSRB	Stator Slot Rotor Bar
FE	Finite Element
DOE	Design of Experiment
NEDC	New European Driving Cycle
US06	A specific test cycle
WLTP	Worldwide Harmonized Light Vehicle Test Procedure
EUDC	Extra-Urban Driving Cycle
IPM	Interior Permanent Magnet
IM	Induction Machine
ID	Irreversible demagnetization
PM	Permanent Magnet
ELU	Environmental Load Units

LCA	Life Cycle Assessment
REM	Rare Earth Material
M	Vehicle Mass
$t_a$	Acceleration Time
$\rho$	Air Density
$C_D$	Drag Coefficient
$f_r$	Rolling Resistance Coefficient
$A_f$	Frontal Area
$\delta$	Mass Correction Factor
$V_b$	Base Speed of the Motor
$\eta$	Efficiency of the Transmission System
$\delta_1$ and $\delta_2$	Coefficients Related to the Rotating Inertial Moment of the Wheels and Power Plant
V	Vehicle Speed
$P_t$	Required Power of the Electric Machine
$D_{os}$	Stator outer diameter
L	Rotor axial length
$I_{max}$	Maximum current
$V_{DC}$	DC Link Voltage
EWG50/50	The Mixture of Ethylene Glycol with Water
$R_b$	Number of Rotor Bars
z	Any Positive Integer
$S_s$	Number of Stator Slots
m	Number of Phases
p	Pair of Poles
q	Number of Slots per Phase per Pole
$k_d$	Winding Distribution Coefficient
$k_p$	Winding Pitch Coefficient
$k_w$	Winding Factor
$\alpha$	Angle Between Two Adjacent Slots
n	Number of Slots Per Pole
$\gamma$	Step Shortness Factor
LPM	Lumped Parameter Model
$k_h$	Coefficients of Hysteresis Losses
$k_e$	Coefficients of Eddy Current Losses
$k_a$	Coefficients of Additional Losses
f	Electric Frequency
$B_m$	Amplitude of the Magnetic Flux Density
$\omega_1, \omega_2,$ and $\omega_3$	Weighted Sum Coefficient
E	Consumed Energy
$T_{ave}$	The Average Temperature of the Coils
$I_{ave}$	Average Input Current
j	Number of Observations in K-means Clustering Method
k	Number of K-means Clusters
S	K-means Clustering Sets
$\mu_i$	Mean of the Points in the of set $S_i$
S/N	Signal to Noise
OA	Orthogonal Array
SA	Sensitivity Analysis
$B_{r0}$	Bar Opening Width
$B_{r1}$	Bar Opening Radius
$H_e$	End Ring Width
$H_{r01}$	Bar Opening Depth
$H_{r2}$	Bar Depth
v	Number of Repeats in Each Experiment

$B_{s0}$	Stator Slot Opening Width
$H_{s0}$	Stator Slot Opening Depth
$H_{s1}$	Stator Slot Opening Depth
$H_{s2}$	Stator Slot Depth
$R_s$	Stator Slot Bottom Radius
$T_w$	Stator Tooth Width
$Eff$	Efficiency
$Pf$	Power Factor
$P_{loss,r}$	Rotor Ohmic Losses
VMS	Von Mises Stress
FOS	Factor of Safety

## Appendix A The Winding Patterns of the Optimum Designs

The linear winding patterns of optimum designs and the corresponding magnetic motive force (MMF) distribution are presented in Figure A1.

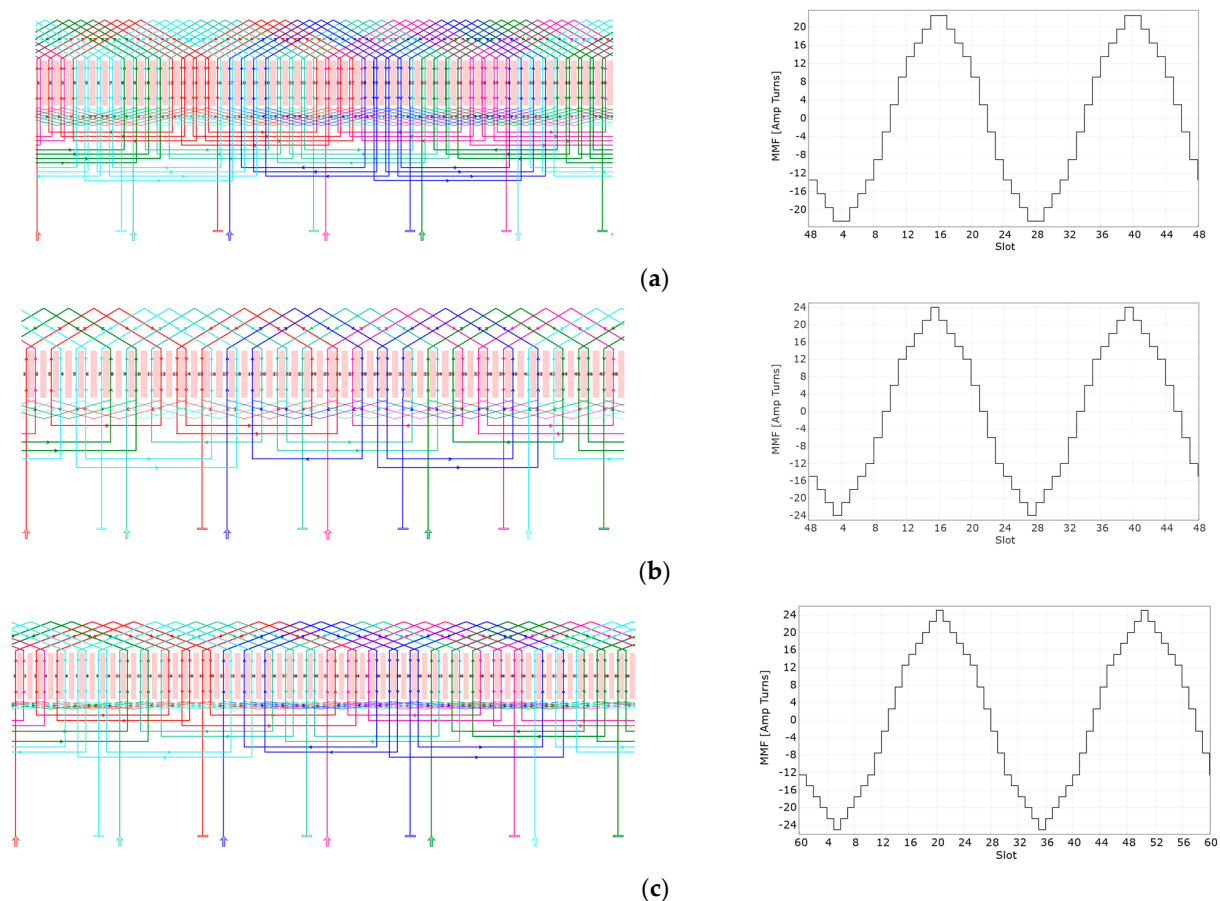


**Figure A1.** The linear winding patterns of optimum designs and the corresponding magnetic motive force (MMF) distribution: (a) S48R58, (b) S48R62, and (c) S60R74.

## References

1. Mahmouditabar, F.; Vahedi, A.; Takorabet, N. Design and Analysis of Interior Permanent Magnet Motor for Electric Vehicle Application Considering Irreversible Demagnetization. *IEEE Trans. Ind. Appl.* **2022**, *58*, 284–293. [[CrossRef](#)]
2. Yang, Z.; Shang, F.; Brown, I.P.; Krishnamurthy, M. Comparative study of interior permanent magnet, induction, and switched reluctance motor drives for EV and HEV applications. *IEEE Trans. Transp. Electrification* **2015**, *1*, 245–254. [[CrossRef](#)]
3. Pellegrino, G.; Vagati, A.; Boazzo, B.; Guglielmi, P. Comparison of induction and PM synchronous motor drives for EV application including design examples. *IEEE Trans. Ind. Appl.* **2012**, *48*, 2322–2332. [[CrossRef](#)]
4. Thangavel, S.; Mohanraj, D.; Girijaprasanna, T.; Raju, S.; Dhanamjayulu, C.; Muyeen, S.M. A Comprehensive Review on Electric Vehicle: Battery Management System, Charging Station, Traction Motors. *IEEE Access* **2023**, *11*, 20994–21019. [[CrossRef](#)]

5. Ajamloo, A.M.; Ibrahim, M.N.; Sergeant, P. Design, Modelling and Optimization of a High Power Density Axial Flux SRM with Reduced Torque Ripple for Electric Vehicles. *Machines* **2023**, *11*, 759. [CrossRef]
6. Mahmouditabar, F.; Vahedi, A.; Marignetti, F. The Demagnetization Phenomenon in PM Machines; Principles, Modelling, and Design Considerations. *IEEE Access* **2023**, *11*, 47750–47773. [CrossRef]
7. ISO 14044:2006; Environmental Management—Life Cycle Assessment—Requirements and Guidelines. International Organization for Standardization: Geneva, Switzerland, 2006. Available online: <https://www.iso.org/standard/38498.html> (accessed on 24 December 2023).
8. ISO 14008:2019; Monetary Valuation of Environmental Impacts and Related Environmental Aspects. International Organization for Standardization: Geneva, Switzerland, 2019. Available online: <https://www.iso.org/standard/43243.html> (accessed on 24 December 2023).
9. EPS Weighting Factors—Version 2020d—IVL.se. Available online: <https://www.ivl.se/english/ivl/publications/publications/eps-weighting-factors---version-2020d.html> (accessed on 30 March 2023).
10. Raghuraman, B.; Nategh, S.; Sidiropoulos, N.; Petersson, L.; Boglietti, A. Sustainability Aspects of Electrical Machines for E-Mobility Applications Part I: A Design with Reduced Rare-earth Elements. In Proceedings of the IECON 2021—47th Annual Conference of the IEEE Industrial Electronics Society, Toronto, ON, Canada, 13–16 October 2021. [CrossRef]
11. SEIA. Critical Materials for Sustainable Energy Applications. Available online: <https://www.seia.org/research-resources/critical-materials-sustainable-energy-applications> (accessed on 30 March 2023).
12. Mahmouditabar, F.; Vahedi, A.; Takorabet, N. Robust Design of BLDC Motor Considering Driving Cycle. *IEEE Trans. Transp. Electrification* **2023**. [CrossRef]
13. Lazari, P.; Wang, J.; Chen, L. A computationally efficient design technique for electric-vehicle traction machines. *IEEE Trans. Ind. Appl.* **2014**, *50*, 3203–3213. [CrossRef]
14. Carraro, E.; Morandini, M.; Bianchi, N. Traction PMASR motor optimization according to a given driving cycle. *IEEE Trans. Ind. Appl.* **2016**, *52*, 209–216. [CrossRef]
15. Li, Q.; Fan, T.; Wen, X.; Li, Y.; Wang, Z.; Guo, J. Design optimization of interior permanent magnet synchronous machines for traction application over a given driving cycle. In Proceedings of the IECON 2017—43rd Annual Conference of the IEEE Industrial Electronics Society, Beijing, China, 29 October–1 November 2017; IEEE: Piscataway, NJ, USA, 2017; pp. 1900–1904. [CrossRef]
16. Chen, H.; Liu, X.; Demerdash, N.A.O.; El-Refai, A.M.; Chen, Z.; He, J. Computationally efficient optimization of a five-phase flux-switching PM machine under different operating conditions. *IEEE Trans. Veh. Technol.* **2019**, *68*, 6495–6508. [CrossRef]
17. Salameh, M.; Brown, I.P.; Krishnamurthy, M. Fundamental Evaluation of Data Clustering Approaches for Driving Cycle-Based Machine Design Optimization. *IEEE Trans. Transp. Electrification* **2019**, *5*, 1395–1405. [CrossRef]
18. Fatemi, A.; Ionel, D.M.; Popescu, M.; Chong, Y.C.; Demerdash, N.A.O. Design Optimization of a High Torque Density Spoke-Type PM Motor for a Formula e Race Drive Cycle. *IEEE Trans. Ind. Appl.* **2018**, *54*, 4343–4354. [CrossRef]
19. Krasopoulos, C.T.; Beniakar, M.E.; Kladas, A.G. Multicriteria PM motor design based on ANFIS evaluation of EV driving cycle efficiency. *IEEE Trans. Transp. Electrification* **2018**, *4*, 525–535. [CrossRef]
20. López-Torres, C.; Espinosa, A.G.; Riba, J.R.; Romeral, L. Design and optimization for vehicle driving cycle of rare-earth-free SynRM based on coupled lumped thermal and magnetic networks. *IEEE Trans. Veh. Technol.* **2018**, *67*, 196–205. [CrossRef]
21. Dianati, B.; Kahourzade, S.; Mahmoudi, A. Optimization of Axial-Flux Induction Motors for the Application of Electric Vehicles Considering Driving Cycles. *IEEE Trans. Energy Convers.* **2020**, *35*, 1522–1533. [CrossRef]
22. Riviere, N.; Villani, M.; Popescu, M. Optimisation of a High Speed Copper Rotor Induction Motor for a Traction Application. In Proceedings of the IECON 2019—45th Annual Conference of the IEEE Industrial Electronics Society, Lisbon, Portugal, 14–17 October 2019; pp. 2720–2725. [CrossRef]
23. Le Besnerais, J.; Lanfranchi, V.; Hecquet, M.; Brochet, P. Optimal slot numbers for magnetic noise reduction in variable-speed induction motors. *IEEE Trans. Magn.* **2009**, *45*, 3131–3136. [CrossRef]
24. Joksimović, G.; Melecio, J.I.; Tuohy, P.M.; Djurović, S. Towards the optimal ‘slot combination’ for steady-state torque ripple minimization: An eight-pole cage rotor induction motor case study. *Electr. Eng.* **2020**, *102*, 293–308. [CrossRef]
25. Darjazini, A.; Vahedi, A.; Nobahari, A.; Gharehseyed, S. Analysis of electromagnetic torque for induction motors with a novel non-skewed rotor structure. *COMPEL Int. J. Comput. Math. Electr. Electron. Eng.* **2022**, *41*, 238–257. [CrossRef]
26. Gundogdu, T.; Zhu, Z.Q.; Mipo, J.C. Influence of stator slot and pole number combination on rotor bar current waveform and performance of induction machines. In Proceedings of the 2017 20th International Conference on Electrical Machines and Systems, ICEMS 2017, Sydney, NSW, Australia, 11–14 August 2017. [CrossRef]
27. Li, Y.; Li, S.; Sarlioglu, B. Analysis of pulsating torque in squirrel cage induction machines by investigating stator slot and rotor bar dimensions for traction applications. In Proceedings of the 2013 IEEE Energy Conversion Congress and Exposition, ECCE, Denver, CO, USA, 15–19 September 2013; pp. 246–253. [CrossRef]
28. Wang, T.; Zheng, P.; Zhang, Q.; Cheng, S. Design characteristics of the induction motor used for hybrid electric vehicle. *IEEE Trans. Magn.* **2005**, *41*, 505–508. [CrossRef]
29. Akhtar, M.J.; Behera, R.K. Optimal design of stator and rotor slot of induction motor for electric vehicle applications. *IET Electr. Syst. Transp.* **2019**, *9*, 35–43. [CrossRef]
30. Roshandel, E.; Mahmoudi, A.; Soong, W.L.; Kahourzade, S. Optimal Design of Induction Motors Over Driving Cycles for Electric Vehicles. *IEEE Trans. Veh. Technol.* **2023**, *72*, 15548–15562. [CrossRef]

31. Popescu, M.; Di Leonardo, L.; Fabri, G.; Volpe, G.; Riviere, N.; Villani, M. Design of Induction Motors with Flat Wires and Copper Rotor for E-Vehicles Traction System. *IEEE Trans. Ind. Appl.* **2023**, *59*, 3889–3900. [[CrossRef](#)]
32. Tran, T.V.; Negre, E.; Mikati, K.; Pellerey, P.; Assaad, B. Optimal design of tefc induction machine and experimental prototype testing for city battery electric vehicle. *IEEE Trans. Ind. Appl.* **2020**, *56*, 635–643. [[CrossRef](#)]
33. Ehsani, M.; Gao, Y.; Emadi, A. Modern Electric, Hybrid Electric, and Fuel Cell Vehicles: Fundamentals, Theory, and Design. In *Modern Electric, Hybrid Electric, and Fuel Cell Vehicles: Fundamentals, Theory, and Design*, 2nd ed.; CRC Press: Boca Raton, FL, USA, 2017; pp. 1–535.
34. Joksimovic, G.; Mezzarobba, M.; Tassarolo, A.; Levi, E. Optimal Selection of Rotor Bar Number in Multiphase Cage Induction Motors. *IEEE Access* **2020**, *8*, 135558–135568. [[CrossRef](#)]
35. Hamdi, E.S. *Design of Small Electrical Machines*; Wiley: New York, NY, USA, 1994; 260p.
36. Pyrhönen, J.; Jokinen, T.; Hrabovcová, V. *Design of Rotating Electrical Machines*; Wiley: New York, NY, USA, 2013. [[CrossRef](#)]
37. Richter, R. *Electrical Machines*; Springer: Berlin/Heidelberg, Germany, 1953; ISBN 978-3-0348-4063-7. Available online: <https://www.orellfuessli.ch/shop/home/artikeldetails/A1033733653> (accessed on 15 July 2023).
38. Qi, J.; Hua, W.; Zhang, H. Thermal Analysis of Modular-Spoke-Type Permanent-Magnet Machines Based on Thermal Network and FEA Method. *IEEE Trans. Magn.* **2019**, *55*, 8104105. [[CrossRef](#)]
39. Nasiri-Zarandi, R.; Ghaheri, A.; Abbaszadeh, K. Thermal Modeling and Analysis of a Novel Transverse Flux HAPM Generator for Small-Scale Wind Turbine Application. *IEEE Trans. Energy Convers.* **2020**, *35*, 445–453. [[CrossRef](#)]
40. Mahmouditabar, F.; Vahedi, A.; Mosavi, M.R.; Bafghi, M.H.B. Sensitivity analysis and multiobjective design optimization of flux switching permanent magnet motor using MLP-ANN modeling and NSGA-II algorithm. *Int. Trans. Electr. Energy Syst.* **2020**, *30*, e12511. [[CrossRef](#)]
41. Gharehseyed, S.; Vahedi, A.; Nobahari, A.; Darjazini, A. Torque characteristics enhancement of ring winding axial flux permanent magnet generator for direct-drive wind turbine. *IET Electr. Power Appl.* **2020**, *14*, 1584–1591. [[CrossRef](#)]

**Disclaimer/Publisher’s Note:** The statements, opinions and data contained in all publications are solely those of the individual author(s) and contributor(s) and not of MDPI and/or the editor(s). MDPI and/or the editor(s) disclaim responsibility for any injury to people or property resulting from any ideas, methods, instructions or products referred to in the content.